Particles II

Access the latest eBook →

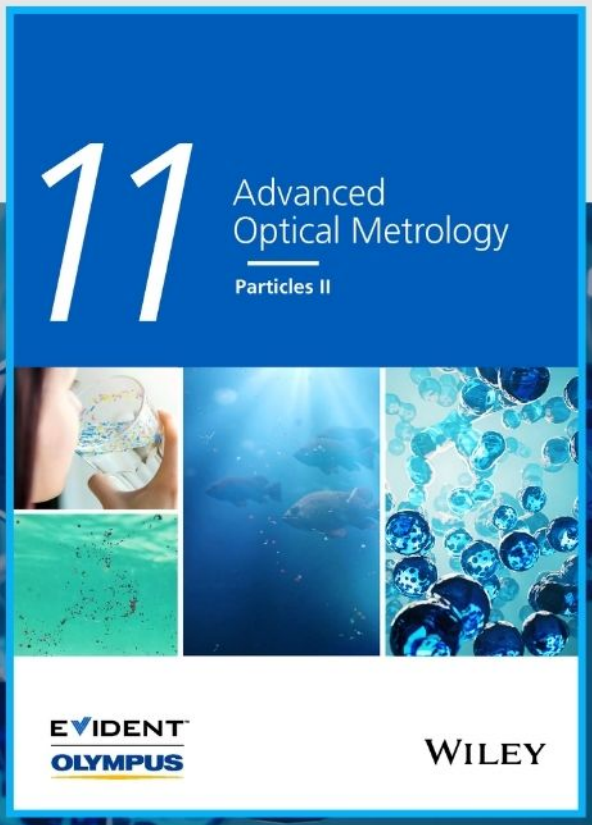

Impact on Biological Systems and the Environment

This eBook is dedicated to the research of Professor David Wertheim.
In collaboration with various groups, Professor Wertheim uses confocal microscopy to analyse the impact of different types of particles on human health and the environment, with a focus on human health-hazardous particles detected with solid-state nuclear track detectors (SSNTD). Download for free, today.

EVIDENT
OLYMPUS

WILEY

ADVANCED FUNCTIONAL MATERIALS
www.afm-journal.de

Solution-Processed Wafer-Scale Ag_2S Thin Films: Synthesis and Excellent Charge Transport Properties

Junren Wang, Shuai Fu, Heng Zhang, Robert Graf, Henry Halim, Shuai Chen, Wenhao Zheng, Mischa Bonn, Katharina Landfester, Andreas Riedinger, and Hai I. Wang**

Monoclinic α-Ag_2S is an intriguing member of transition metal sulfides with great potential for all-inorganic flexible optoelectronics and thermoelectrics. Fabrication of large-area, high-quality α-Ag_2S thin films and understanding their charge transport properties are critical for device operations yet have remained largely unexplored. Here, a novel two-step, the solution-processed approach is reported to produce wafer-sized, highly crystalline α-Ag_2S thin films. Ultrafast terahertz (THz) conductivity measurements reveal that photogenerated charge carriers undergo efficient band transport, with room-temperature mobility of ≈150 $cm^2\ V^{-1}\ s^{-1}$ and a diffusion length exceeding 500 nm. Furthermore, introducing poly(vinyl alcohol) (PVA) as the rigid component into the aqueous silver thiolate precursor enables the synthesis of free-standing α-Ag_2S thin films with a mobility of ≈35 $cm^2\ V^{-1}\ s^{-1}$, demonstrating their potential for flexible optoelectronics. This study provides a facile synthesis route for high-quality, large-area α-Ag_2S thin films with good charge transport properties, relevant for their integration into optoelectronics and wearable electronics.

1. Introduction

Monoclinic α-Ag_2S is a representative transition metal sulfide (TMS) with extraordinary ductility resembling metals due to the high cleavage energy between the adjacent crystal planes.[1] The unique combination of its metal-like ductility and relatively high intrinsic mobility (over 100 $cm^2\ V^{-1}\ s^{-1}$)[1a] renders α-Ag_2S as potential active components for flexible optoelectronics. For instance, Jo et al.[2] pioneered the solution-processed synthesis of ductile semiconducting Ag_2S thin films with remarkable stretchability as high as 14.9%, enabling wrinkled Ag_2S-based memory devices with excellent mechanical stretchability and their further integration with motion sensors to form self-powered healthcare monitoring systems. Furthermore, α-Ag_2S has also attracted considerable attention for thermoelectrics due to the high Seebeck coefficient.[3]

Besides its great potential for flexible electronics and thermoelectrics, α-Ag_2S has been long considered as promising light absorbers for low-cost and efficient optoelectronics, including thin-film solar cells, since the first research surge of TMSs for photovoltaics in the 1980s.[4] The advantage of α-Ag_2S for optoelectronics is that it combines fascinating properties, including non-toxic elements, a suitable direct bandgap (with an energy gap of 0.9–1.1 eV)[5,6] for photovoltaics, and an extremely high absorption coefficient.[7] Within the theoretical framework developed by Shockley and Queisser, the maximum efficiency of a single junction solar cell based on α-Ag_2S can reach up to ≈30%.[8] Despite its great promise, α-Ag_2S has attracted little research attention compared to other TMS materials such as pyrite, and the conversion efficiency of Ag_2S-based photovoltaic devices remains quite moderate with the state-of-the-art value of around 3%.[9] The origin for the relatively low energy conversion efficiency of α-Ag_2S solar cells may be attributed to relatively high defect densities, as reported for some of other TMS materials.[10]

Therefore, to realize the full potential of α-Ag_2S for the above applications, producing high-quality thin films with relatively low defect density and excellent charge transport properties (e.g., high carrier mobility) is mandatory. Over the past decades, several methods have been developed to prepare Ag_2S thin films, such as chemical bath deposition (CBD),[11] epitaxial growth,[12] chemical vapor deposition,[13] spray pyrolysis,[14] and electrodeposition.[15] Despite these efforts, the production of high-quality, large-scale α-Ag_2S thin films in a facile manner remains challenging, impeding the development of relevant devices and applications. Furthermore, understanding the charge transport properties in α-Ag_2S is essential for device operations, yet has remained largely unexplored.

Here we develop a two-step, solution-processed wafer-scale deposition of α-Ag_2S thin films with high charge carrier mobility and long charge carrier diffusion length (over 500 nm). We employ water-soluble silver thiolate (i.e., Ag-3-mercaptopropionic acid (Ag-MPA)) as the precursor, which can be easily

J. Wang, S. Fu, H. Zhang, R. Graf, H. Halim, S. Chen, W. Zheng, M. Bonn, K. Landfester, A. Riedinger, H. I. Wang
Max Planck Institute for Polymer Research
Ackermannweg 10, 55128 Mainz, Germany
E-mail: riedinger@mpip-mainz.mpg.de; wanghai@mpip-mainz.mpg.de
The ORCID identification number(s) for the author(s) of this article can be found under https://doi.org/10.1002/adfm.202113147.

DOI: 10.1002/adfm.202113147

processed into uniform silver thiolate films with a controllable thickness (from 30 to 200 nm). Following the pyrolysis of the silver thiolate, a continuous and highly crystalline Ag_2S film is readily obtained. We perform time- and frequency-resolved photoconductivity measurements by ultrafast THz spectroscopy to investigate their charge transport properties. The results reveal high mobility of ≈150 $cm^2\ V^{-1}\ s^{-1}$, and a charge carrier diffusion length over 500 nm, exceeding the optical penetration depth that determines the photogenerated charge carrier distribution (e.g., ≈300 nm at 3.1 eV). The latter condition ensures that the majority of charge carriers can circumvent the trapping process to reach the electrodes for thin-film photovoltaic applications following light absorption. Intriguingly, the photoconductivity of α-Ag_2S is found to increase strongly with decreasing temperature. This indicates a band-like charge transport mechanism in our samples and suggests a minor role of defect scattering in determining the charge carrier conductivity (and thus the high quality of our sample). Finally, we show that our synthetic method can be further extended to synthesize free-standing α-Ag_2S thin films with satisfactory mobility of ≈35 $cm^2\ V^{-1}\ s^{-1}$, demonstrating their great potential for flexible optoelectronics. Our study provides a facile strategy for fabricating high-quality (i.e., low defect density and high carrier mobility) and large-area α-Ag_2S thin films. The efficient charge transport in α-Ag_2S paves the way for the integration of α-Ag_2S thin films toward optoelectronics and wearable electronics.

2. Results and Discussion

As schematically shown in **Figure 1**a, we realize the solution-processed synthesis of α-Ag_2S by using Ag-MPA as the precursor. Firstly, $Ag(NO)_3$ was mixed with MPA in ethylene glycol (EG) and diethylene glycol (DEG). Following a purification step, the synthesized Ag-MPA can be further dispersed into water to form Ag-MPA aqueous solution.[16] The Ag-MPA precursors were then spin-coated on the substrate of interest to form an Ag-MPA thin film (Figure 1b), which converts into monoclinic α-Ag_2S thin film upon pyrolysis (Figure 1c).

The X-ray diffraction (XRD) pattern of Ag-MPA films (with a thickness of 500 nm) shows periodic diffraction peaks at $2\theta = 4°$, 8°, and 12° (Figure 1d), which correspond to the (010), (020), and (030) facets, respectively. This indicates that Ag-MPA comprises lamellar structures with an interlayer spacing of ≈2 nm between the adjacent Ag-S layers. To shed light on the structure of Ag-MPA, we conducted solid-state NMR spectroscopy (see Figure S1, Supporting Information). We found that around 50% MPA ligands are distributed perpendicular to the Ag-S layers in the *trans* conformation, whereas the other half of MPA ligands are distributed almost parallel to the Ag-S layers in the *gauche* conformation (as shown in Figure 1b). The terminal carboxyl group of MPA ligands coordinates with the hydroxyl group of EG or DEG by hydrogen bonding. The hydroxyl groups contribute to the excellent water-solubility of the silver thiolate precursor. Upon heating the Ag-MPA thin film at 180 °C for 15 min, the characteristic peaks of Ag-MPA disappear with the emergence of the crystalline peaks of monoclinic α-Ag_2S (Figure 1d). Based on thermogravimetric (TG) measurement, we show that the decomposition from the Ag-MPA to α-Ag_2S starts from ≈170 °C (see Figure S2, Supporting Information). In addition, based on the XPS study (see Figure S3, Supporting Information), we can conclude that over ≈90% of the sulfur belongs to Ag_2S, indicating a relatively complete transformation. Further effort in controlling annealing conditions (e.g., time and temperature) to optimize the crystallization process and further decrease the MPA residuals is required. Based on the Tauc plot analysis, we estimate the bandgap of α-Ag_2S thin film (Figure 1e) to be ≈1.3 eV, close to the theoretically predicted bandgaps ranging from 0.9 to 1.1 eV.[5,6]

The formation and morphology of α-Ag_2S were further examined by high-resolution transmission electron microscopy (HRTEM) (Figure 1f), atomic force microscopy (AFM) (Figure 1g and Figure S4, Supporting Information), and scanning electron microscopy (SEM) (Figure S5, Supporting Information). The HRTEM image (Figure 1f) reveals lattice fringes with an interplanar spacing of 2.4 Å, which matches well with the distance between the adjacent (013) planes of α-Ag_2S (PDF 14-0072). Thanks to the high solubility of Ag-MPA and the mild crystallization process, AFM images of α-Ag_2S thin film (Figure 1g and Figure S4, Supporting Information) exhibits a relatively smooth surface with a root mean square (RMS) surface roughness of 11 nm (for a film of 200 nm thick), and a lateral diameter of ≈2.5 cm, demonstrating their potential for device-relevant applications. The top and cross-section SEM images (Figure S5, Supporting Information) reveal that the samples are pinhole-free, and have relatively smooth surfaces. The thickness of the Ag_2S thin film can be readily increased by repeating the spin-coating and heating processes (at least up to ≈1.5 µm as shown in Figure S6, Supporting Information). We find that increasing the film thickness does not impact on the photoconductivity amplitude and dynamics (see Figure S7, Supporting Information).

To shed light on microscopic charge transport properties of Ag-MPA and α-Ag_2S thin films, we employed ultrafast optical pump-THz probe (OPTP) spectroscopy to probe their time- and frequency-resolved photoconductivity. As an all-optical technique, OPTP spectroscopy accesses the conductivity of materials of interest in a contact-free fashion, and thus is particularly powerful for exploring the nature of charge transport in nanomaterials.[17] In a typical OPTP measurement, an ultrafast (≈100 fs duration) laser pulse of 3.1 eV optically injects charge carriers into Ag-MPA (as a control measurement) and α-Ag_2S thin films (with a thickness of ≈200 nm; see Figure S4, Supporting Information) following the interband excitation. Subsequently, a single-cycle THz pulse (≈1 ps duration) drives the conduction of photogenerated free charge carriers by the oscillating THz electric field E. This leads to THz attenuation due to free carrier absorption. The relative change of the THz electric field ($-\Delta E/E$) is proportional to the photoconductivity $\Delta\sigma$ following the thin-film approximation (Equation (1)):[18]

$$\Delta\sigma = -\frac{n+1}{Z_0 \cdot l} \cdot \frac{\Delta E}{E} \tag{1}$$

where $n = 1.95$ represents the refractive index of the fused silica substrate in the measured THz range (0.5–2 THz), $Z_0 = 377\ \Omega$ is the impedance of free space, and l is the optical penetration depth.

Figure 2a compares the photoconductivity dynamics of Ag-MPA and α-Ag_2S thin films at the same absorbed photon

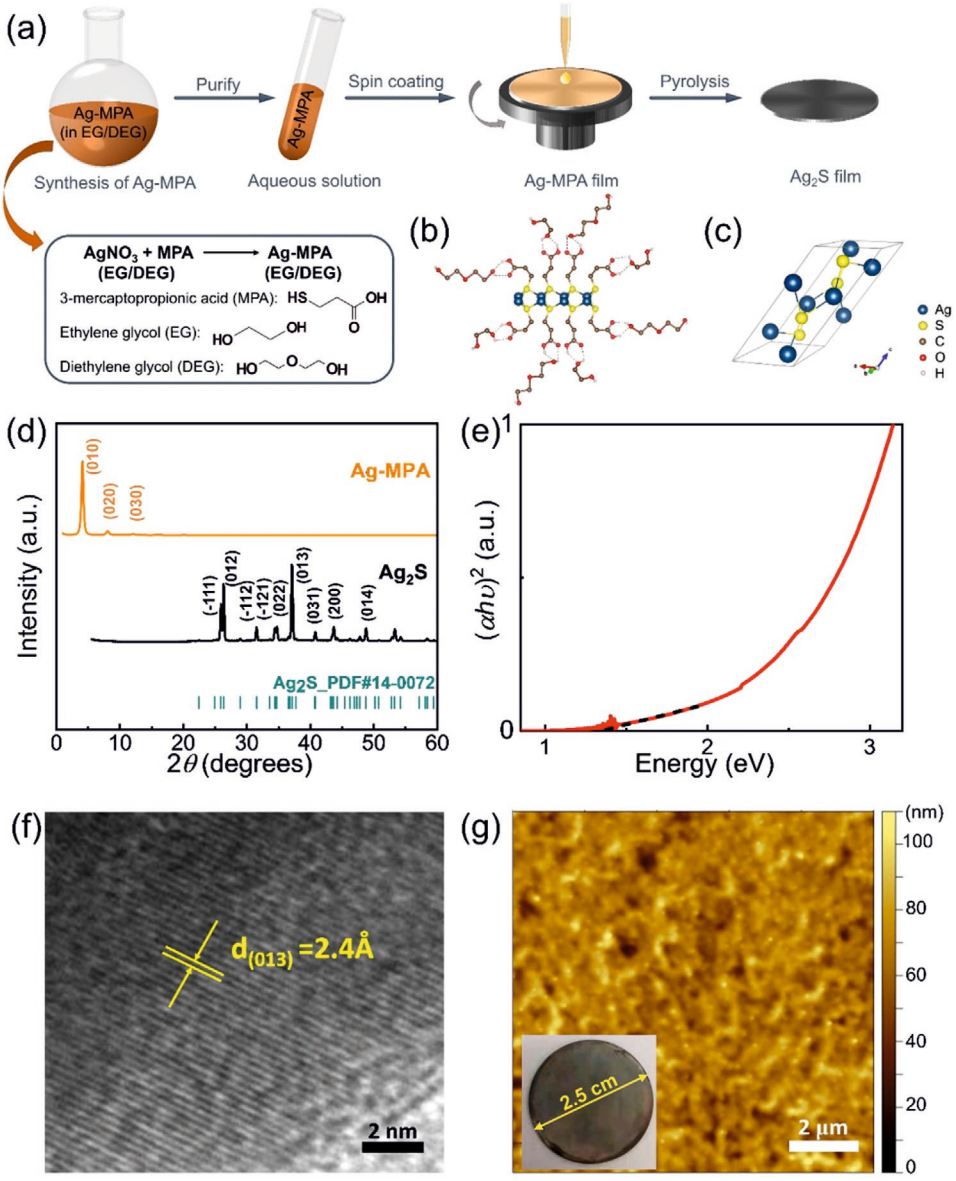

Figure 1. Synthesis and characterizations of Ag-MPA and Ag_2S thin films. a) Schematic presentation of solution-processed synthesis of Ag-MPA and Ag_2S thin films. Schematic representation of the crystal structures of b) Ag-MPA (hydrogen atoms connected to carbons are omitted) and c) Ag_2S (space group $P2_1/c$). d) XRD patterns of Ag-MPA (orange), Ag_2S (black) and the reference pattern of PDF 14-0072 (green). e) Tauc plot of Ag_2S thin film. f) HRTEM image of Ag_2S. g) AFM image of Ag_2S thin film. Inset is a picture of Ag_2S thin film supported on the fused silica substrate with a diameter of ≈2.5 cm.

density of ≈3.4 × 10^{14} cm^{-2}. Upon excitation, the optically injected charge carriers in Ag-MPA thin films exhibit poor photoconductivity of ≈20 S m^{-1} in the peak, followed by a fast decay process within ≈1 ps. The rapid photoconductivity decay may be tentatively assigned to the charge localization process (e.g., by trapping). By contrast, photogenerated charge carriers in α-Ag_2S thin films possess much higher photoconductivity of ≈6000 S m^{-1} (≈300 times higher than that of Ag-MPA) and a substantially longer lifetime (as shown below), demonstrating their potential for photovoltaic and optoelectronic applications. To further elucidate their charge transport properties, we measured the frequency-resolved complex photoconductivity for α-Ag_2S (Figure 2b) and Ag-MPA (Figure 2c) thin films at ≈1 ps after their maximum photoconductivity. The frequency-resolved complex photoconductivities can be phenomenologically described by the Drude-Smith (DS) model. In the model, the motion of charge carriers in the samples is subject to backscattering (e.g., at grain boundaries), following (Equation (2)):[17,19]

$$\Delta\sigma(\omega) = \frac{\omega_p^2 \varepsilon_0 \tau}{1 - i\omega\tau}\left(1 + \frac{c}{1 - i\omega\tau}\right) \quad (2)$$

where ω_p, τ, ε_0 denote the plasma frequency, effective carrier scattering time, and vacuum permittivity, respectively. The

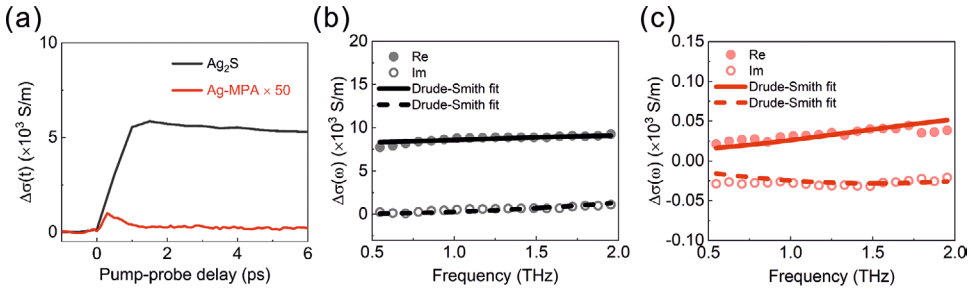

Figure 2. THz photoconductivity of Ag_2S and Ag-MPA thin films. a) Time-resolved THz photoconductivity of Ag_2S thin film (black line) and Ag-MPA thin film (red line, multiplied by 50). Samples are excited by a 3.1 eV laser pulse with the same absorbed photon density of ≈3.4×10^{14} cm^{-2}, and their photoconductivity is probed by a single-cycle THz pulse under N_2 atmosphere. Frequency-resolved THz photoconductivity of b) Ag_2S thin film and c) Ag-MPA thin film measured at ≈1 ps after the maximum photoconductivity. The solid and dashed lines represent the Drude-Smith model describing the real and imaginary components of the complex THz photoconductivity, respectively.

parameter c parameterizes the probability of backscattering, with values spanning from 0 (for isotropic scattering) to −1 (for preferential scattering). The DS fit to the data yields τ of 39 ± 2 and 42 ± 4 fs, and c parameters of −0.49 ± 0.01 and −0.92 ± 0.02 for α-Ag_2S and Ag-MPA thin films, respectively. Given the inferred scattering time τ and c, together with the effective charge carrier mass obtained from reference ($m^* = 0.23$ m_0),[20] we estimate the mobility (μ) of α-Ag_2S thin film to be ≈150 cm^2 V^{-1} s^{-1} in the dc limit following $\mu = \frac{e\tau}{m^*} \times (1+c)$, where e is the elementary charge. The estimated μ is in good agreement with the reported device-relevant mobility,[1a] representing one of the highest values for chalcogenide-based inorganic semiconducting materials (all quantified by THz spectroscopy, see Table S1, Supporting Information). Furthermore, THz measurements at four different sample spots show similar peak photoconductivities and lifetimes (Figure S8, Supporting Information), demonstrating the uniformity of the film.

Along with the remarkably high charge mobility, another figure of merit of a material for photovoltaic applications is the long charge carrier lifetime, or equivalently, low decay rate. To unveil the charge decay rates associated with different recombination channels (trapping, bimolecular recombination, and Auger recombination) in α-Ag_2S, we measured photoconductivity dynamics for its thin film under various incident pump fluences ranging from 4.4 to 82.5 μJ cm^{-2}. As shown in **Figure 3**a, the photoconductivity decays faster at elevated pump fluences, as a result of the increasing contributions from the higher-order decay channels (e.g., bimolecular and Auger recombination).[21] To clarify the dependence of decay rates on the charge carrier density, we globally fit the pump fluence-dependent photoconductivity dynamics with the coupled rate equation (Equation (3)):

$$\frac{dn(t)}{dt} = -k_1 n - k_2 n^2 - k_3 n^3 \quad (3)$$

where $n(t)$ is the charge carrier density at the pump-probe delay t, k_1 represents the monomolecular recombination rate coefficient accounting for the trapping-related process, k_2 stands for the bimolecular recombination rate coefficient originating from the recombination of electron–hole pairs, and k_3 denotes the Auger recombination rate coefficient. Based on the fitting, k_1, k_2, and k_3 are extracted to be 2.08 × 10^8 s^{-1}, 7.13 × 10^{-10} cm^3 s^{-1} and 1.19 × 10^{-29} cm^6 s^{-1}, respectively. This gives rise to the total decay rate (R_{total}), by weighting the contribution of different recombination channels, as shown in Figure 3b (black line) as a function of absorbed photon density. By knowing the high charge mobility μ and the recombination rate R_{total}, we can further calculate the diffusion length L in α-Ag_2S thin film following (Equation (4)):

$$L(n) = \sqrt{\frac{D}{R_{total}(n)}}, \text{ with } D = \frac{\mu k_B T}{e} \quad (4)$$

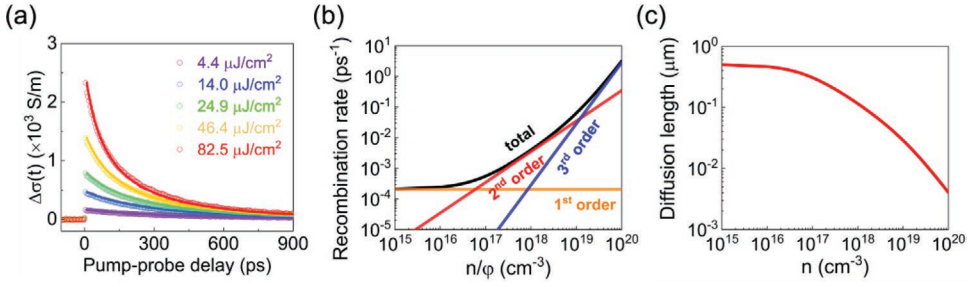

Figure 3. Charge carrier dynamics of Ag_2S thin films at various initial charge carrier concentrations. a) Fluence-dependent THz photoconductivity dynamics of Ag_2S thin film following 3.1 eV excitations, with incident pump fluences ranging from 4.4 to 82.5 μJ cm^{-2}. The solid lines represent global fitting to the recombination rates equation as discussed in the main text. The recombination rates k_1, k_2, and k_3 are extracted to be 2.08 × 10^8 s^{-1}, 7.13 × 10^{-10} cm^3 s^{-1}, and 1.19 × 10^{-29} cm^6 s^{-1}, respectively. b) Charge carrier recombination rates of Ag_2S thin films at varied charge carrier concentrations. Here φ stands for the photon-to-charge conversion ratio representing the number of charge carriers created per absorbed photon. c) Charge carrier diffusion length of Ag_2S thin films as a function of charge carrier concentration.

where k_B and T stand for the Boltzmann constant and temperature, respectively. Figure 3c plots the lower bound limit of L as a function of carrier density by assuming the photon-to-charge branching ratio $\phi = 1$. We found that the lower bound limit of L is already around 500 nm, following a relatively low excitation fluence that is relevant for practical applications ($<10^{17}$ cm^{-3}). To demonstrate their potential in optoelectronic applications, here we compare the characteristic charge carrier properties of α-Ag_2S with the state-of-the-art solution-processed materials for photovoltaic applications (e.g., organic-inorganic hybrid perovskites; see Table S2, Supporting Information). While α-Ag_2S shows an unfavorably (1–2 orders of magnitude) higher recombination rate than those of perovskites, it possesses an order of magnitude larger charge carrier mobility. By balancing these two parameters for charge transport, the charge carrier diffusion length of α-Ag_2S is found to be close to those of perovskites (≈1 µm). More importantly, the inferred carrier diffusion length, in spite of being underestimated, is already much longer than the penetration depth (≈300 nm at 3.1 eV) of excitation photons for α-Ag_2S. This favorable condition indicates that for thin-film α-Ag_2S devices, e.g., with a thickness of 500 nm (see Figure S9, Supporting Information), the majority of photogenerated charge carriers can be collected by electrodes without significant trap-mediated carrier loss, mainly thanks to the high charge carrier mobility and high absorption coefficient of the α-Ag_2S. Figure S10 (Supporting Information) demonstrates that the Ag_2S film thickness can be increased to 1 µm to guarantee absorption exceeding 95% at the band-edge. Given that our inferred lower limit of the diffusion length of 500 nm is already close to 1 µm, our studies seem relevant for the photovoltaic community.

To provide more insights into the charge transport mechanism, we record temperature (T)-dependent photoconductivity dynamics for α-Ag_2S thin film from 350 to 78 K. In principle, the measured photoconductivity is proportional to the product of the density (n) and mobility (μ) of photogenerated charge carriers. Thanks to the high absorption of α-Ag_2S (over 80% at 3.1 eV), n is expected to change little in the temperature-dependent measurements for α-Ag_2S. Therefore, the charge carrier mobility (and thus charge scattering time) plays a dominant role in dictating the photoconductivity. As shown in **Figure 4**a, the photoconductivity increases with decreasing temperature, revealing a negative temperature coefficient of conductivity (and thus charge carrier mobility), i.e., $\frac{d\mu}{dT} < 0$. This suggests that photogenerated charge carriers are conducted in α-Ag_2S thin films following band-like transport. The power-law fitting ($\Delta\sigma \propto T^{\alpha}$) between the maximum photoconductivity and temperature (Figure 4b) yields a power index α of –1. The obtained strong temperature dependence of conductivity in our sample suggests that phonon scattering dominates the charge transport, and that defect scattering plays a relatively minor role in determining the charge carrier mobility of α-Ag_2S. Overall, the observed high charge carrier mobility and band-like transport underline the high quality of our samples with relatively low defect density.

Finally, we demonstrated that our synthesis strategy can be readily extended to fabricate flexible, freestanding α-Ag_2S thin films with potential applications in flexible (opto-)electronics. For that, we introduced poly(vinyl alcohol) (PVA) to the aqueous Ag-MPA solution. The reasons for choosing PVA in the synthesis are twofold: PVA can be well-blended with the precursor solution, maintaining the solution-processed feature of the approach; and it can host Ag_2S while introducing its flexible mechanical nature to the thin film. Upon pyrolysis, the XRD pattern of Ag_2S-PVA exhibits a broad halo at $2\theta = 19°$ stemming from the amorphous PVA and crystalline peaks originating from α-Ag_2S (**Figure 5**a). The resulting Ag_2S-PVA thin film shows a flat surface with an extremely low surface roughness of ≈635 pm (Figure 5b), a large lateral size of ≈3 cm × 2 cm (Figure 5c), and outstanding structural integrity during bending (Figure 5d). Frequency-resolved complex photoconductivity for the freestanding Ag_2S-PVA thin film can also be well-described by the Drude-Smith model as discussed above, yielding τ of 42 ± 4 fs and c of –0.92 ± 0.02, respectively. Compared to the supported α-Ag_2S film, the addition of PVA leads to an increase in the absolute value of c parameter, while τ remains almost the same within the experimental error. This gives rise to mobility of ≈35 cm^2 V^{-1} s^{-1} in the dc limit, still exceptional for conducting polymers typically used for flexible electronics.[22] The reduced mobility may arise from the disturbed crystallization process of α-Ag_2S and separation of conducting α-Ag_2S domains, as a consequence of introducing

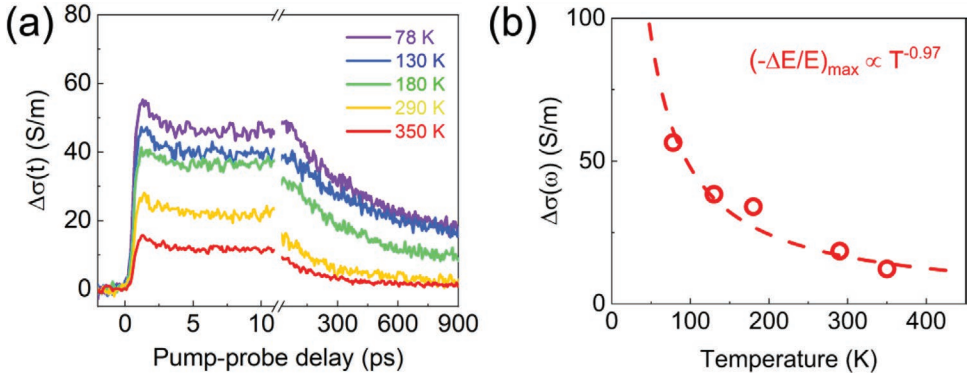

Figure 4. Temperature-dependent THz photoconductivity of Ag_2S thin films. a) Temperature-dependent time-resolved THz photoconductivity dynamics of Ag_2S thin films following 3.1 eV excitation with a fixed incident pump fluence of 1.8 µJ cm^{-2}. b) The maximum THz photoconductivity as a function of temperature. The dashed line represents a power-law description of the data.

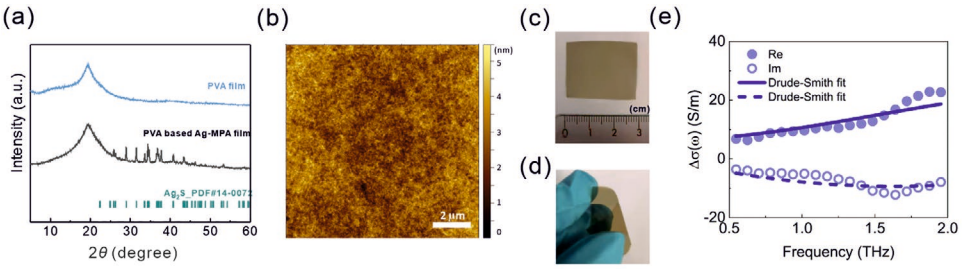

Figure 5. Characterization and THz photoconductivity of Ag_2S-PVA thin films. a) XRD patterns of a pure PVA thin film and an Ag_2S-PVA thin film. b) AFM image of an Ag_2S-PVA thin film. c) A picture of as-synthesized freestanding PVA-Ag_2S thin film with a length of ≈3 cm. d) A picture of bending as-synthesized freestanding PVA-Ag_2S thin film to show the exceptional flexibility. e) Frequency-resolved THz photoconductivity of freestanding PVA-Ag_2S thin film measured at ≈1 ps after the maximum photoconductivity. The sample is excited by a 3.1 eV pulsed laser with an incident pump fluence of 3.3 μJ cm^{-2}. The solid and dashed lines represent the Drude-Smith model describing the real and imaginary components of the complex THz photoconductivity, respectively.

PVA. Further tailoring the relative ratio between the aqueous Ag-MPA solution and PVA and optimizing the crystallization conditions may help to increase the mobility of freestanding Ag_2S-PVA thin films. In addition, composition tuning also offers us a powerful knob to improve the surface quality of Ag_2S layers loaded on the substrate. For instance, we show that one can substantially reduce the surface roughness over 50% from 11 (with no PVA) to ≈5 nm (see Figure S11, Supporting Information) by adjusting the Ag-MPA/PVA ratio (to, e.g., 0.2).

Finally, to (i) investigate the effect of bending on the optoelectronic properties of PVA-Ag_2S films, we perform in situ THz photoconductivity measurements on free standing PVA-Ag_2S thin films (≈25 mm × 15 mm), by controlling the extent of the bending and the number of bending cycles. The measurement is achieved by mounting the two edges of the free-standing PVA-Ag_2S onto a home-designed sample holder, and tuning the lateral distance between the clamps via a translation stage, as schematically shown in Figure S12a (Supporting Information). Figure S12b,c (Supporting Information) shows two images of the free-standing PVA-Ag_2S thin film without and with bending load, respectively. Figure S12d (Supporting Information) demonstrates the photoconductivity dynamics, while their peak values at different bending degrees are summarized in Figure S12e (Supporting Information). As we can see, no obvious photoconductivity change is noticed during the bending (up to ≈25% compression load). This indicates that bending plays a minor role in affecting the optoelectronic properties of the free-standing PVA-Ag_2S thin film. In Figure S12f,g (Supporting Information), we show that over 100 times of bending cycles, no clear drop is seen in the THz photoconductivity. In addition, no obvious crack is noticed after 100 times bending (see Figure S13, Supporting Information), indicating the robustness of PVA-Ag_2S thin film for flexible electronics. Based on these data, we conclude that the PVA-Ag_2S composite is a promising candidate for flexible electronics, which uniquely combines excellent mechanical and electrical properties.

3. Conclusion

In conclusion, we report the solution-processed synthesis of wafer-scale, highly crystalline α-Ag_2S thin films by employing aqueous Ag-MPA as the precursor and investigate their charge transport properties by ultrafast THz spectroscopy. THz photoconductivity measurements reveal that the photogenerated charge carriers migrate in α-Ag_2S thin films by band-like transport with exceptional mobility of ≈150 cm^2 V^{-1} s^{-1}, and a long diffusion length over 500 nm. The synthesis can be further extended to fabricate free-standing α-Ag_2S thin films with decent mobility of ≈35 cm^2 V^{-1} s^{-1}, promising for flexible electronics and optoelectronics. Our study not only provides a facile synthesis route for large-scale, high-quality α-Ag_2S films, but also sheds light on the charge transport mechanism of α-Ag_2S, relevant for potential applications in optoelectronics and wearable electronics.

Supporting Information

Supporting Information is available from the Wiley Online Library or from the author.

Acknowledgements

J.W. and S.F. contributed equally to this work. The authors thank Christoph Sieber for XRD measurements, Kathrin Kirchhoff for HRTEM measurements, Gunnar Glasser for SEM measurements, Petra Räder for TG measurements, Leon Prädel for XPS measurements, Marc-Jan van Zadel and Florian Gericke for designing and fabricating the sample holder for in situ photoconductivity studies of free-standing samples under bending, Jiabao Yang for assisting THz measurements of bent samples. J.W. and S.F. acknowledge fellowship support from China Scholarship Council (CSC). H.H. thanks the support from the Max Planck Graduate Center with the Johannes Gutenberg University in Mainz (MPGC).

Open access funding enabled and organized by Projekt DEAL.

Conflict of Interest

The authors declare no conflict of interest.

Data Availability Statement

The data that support the findings of this study are available from the corresponding author upon reasonable request.

Keywords

α-Ag_2S thin films, band-like transport, charge carrier dynamics, mobility, solution-processed synthesis, THz spectroscopy

Received: December 22, 2021
Revised: March 20, 2022
Published online: April 15, 2022

[1] a) X. Shi, H. Chen, F. Hao, R. Liu, T. Wang, P. Qiu, U. Burkhardt, Y. Grin, L. Chen, *Nat. Mater.* **2018**, *17*, 421; b) G. Li, Q. An, S. I. Morozov, B. Duan, W. A. Goddard, Q. Zhang, P. Zhai, G. J. Snyder, *Npj Comput. Mater.* **2018**, *4*, 44.
[2] S. Jo, S. Cho, U. J. Yang, G.-S. Hwang, S. Baek, S.-H. Kim, S. H. Heo, J.-Y. Kim, M. K. Choi, J. S. Son, *Adv. Mater.* **2021**, *33*, 2100066.
[3] a) G. Kim, D. Byeon, S. Singh, K. Hirata, S. Choi, M. Matsunami, T. Takeuchi, *J. Phys. D* **2021**, *54*, 115503; b) W.-X. Zhou, D. Wu, G. Xie, K.-Q. Chen, G. Zhang, *ACS Omega* **2020**, *5*, 5796.
[4] A. Ennaoui, H. Tributsch, *Sol. Cells* **1984**, *1*, 197.
[5] P. Junod, PhD thesis, ETH, Zurich **1959**.
[6] P. Junod, H. Hediger, B. Kilchör, J. Wullschleger, *Philos. Mag.* **1977**, *36*, 941.
[7] M. Diware, S. Ganorkar, J. Kim, S. Bramhe, H. Cho, Y. Cho, W. Chegal, *Appl. Phys. Lett.* **2015**, *107*, 171905.
[8] W. Shockley, H. J. Queisser, *J. Appl. Phys.* **1961**, *32*, 510.
[9] C. Chen, Y. Zhai, F. Li, G. Yue, *J. Power Sources* **2015**, *298*, 259.
[10] a) S. Ahmmed, A. Aktar, J. Hossain, A. B. M. Ismail, *Sol. Energy* **2020**, *207*, 693; b) G. Paul, S. Chatterjee, A. J. Pal, *Sol. Energy Mater. Sol. Cells* **2018**, *182*, 339; c) J. Vidal, S. Lany, M. d'Avezac, A. Zunger, A. Zakutayev, J. Francis, J. Tate, *Appl. Phys. Lett.* **2012**, *100*, 032104.
[11] a) H. Meherzi-Maghraoui, M. Dachraoui, S. Belgacem, K. Buhre, R. Kunst, P. Cowache, D. Lincot, *Thin Solid Films* **1996**, *288*, 217; b) V. Krylova, A. Milbrat, A. Embrechts, J. Baltrusaitis, *Appl. Surf. Sci.* **2014**, *301*, 134.
[12] a) D. Karashanova, D. Nihtianova, K. Starbova, N. Starbov, *Solid State Ionics* **2004**, *171*, 269; b) H. Haefke, A. Panov, V. Dimov, *Thin Solid Films* **1990**, *188*, 133.
[13] A. Panneerselvam, M. A. Malik, P. O'Brien, J. Raftery, *J. Mater. Chem.* **2008**, *18*, 3264.
[14] H. Dlala, M. Amlouk, S. Belgacem, P. Girard, D. Barjon, *EPJ Appl. Phys.* **1998**, *2*, 13.
[15] X. Y. Guo, S. Y. Cheng, P. M. Lu, H. F. Zhou, *Mater. Sci. Forum* **2011**, *663*, 910.
[16] J. Wang, R. Graf, A. Riedinger, *J. Mater. Chem.* **2021**, *9*, 11079.
[17] R. Ulbricht, E. Hendry, J. Shan, T. F. Heinz, M. Bonn, *Rev. Mod. Phys.* **2011**, *83*, 543.
[18] J. Neu, K. P. Regan, J. R. Swierk, C. A. Schmuttenmaer, *Appl. Phys. Lett.* **2018**, *113*, 233901.
[19] T. L. Cocker, D. Baillie, M. Buruma, L. V. Titova, R. D. Sydora, F. Marsiglio, F. A. Hegmann, *Phys. Rev. B* **2017**, *96*, 205439.
[20] H. P. Geserich, W. Suppanz, *Phys. Status Solidi B* **1969**, *35*, 381.
[21] a) Y. Yang, M. Yang, Z. Li, R. Crisp, K. Zhu, M. C. Beard, *J. Phys. Chem. Lett.* **2015**, *6*, 4688; b) C. Wehrenfennig, G. E. Eperon, M. B. Johnston, H. J. Snaith, L. M. Herz, *Adv. Mater.* **2014**, *26*, 1584.
[22] W. Gao, H. Ota, D. Kiriya, K. Takei, A. Javey, *Acc. Chem. Res.* **2019**, *52*, 523.